Advances in Geo-Energy Research

Vol. 14, No. 3, p. 187-200, 2024

Original article

Accurate structural characterization of nanopores in coal by cryo-FIB-SEM

Gang Wang[1,2]*, Xuechang Chen[1], Gang Wang[3], Houquan Zhang[4], Jing Wang[5], Hao Xu[1]

[1]*College of Safety and Environment Engineering, Shandong University of Science and Technology, Qingdao 266590, P. R. China*

[2]*Mine Disaster Prevention and Control-Ministry of State Key Laboratory Breeding Base, Shandong University of Science and Technology, Qingdao 266590, P. R. China*

[3]*College of Civil Engineering, Fujian University of Technology, Fuzhou 350118, P. R. China*

[4]*State Key Laboratory of Intelligent Construction and Healthy Operation and Maintenance of Deep Underground Engineering, China University of Mining and Technology, Xuzhou 221116, P. R. China*

[5]*School of Qilu Transportation, Shandong University, Jinan 250061, P. R. China*

Keywords:
Nanopores
deep learning
structural characterization
coal seam wetting

Cited as:
Wang, G., Chen, X., Wang, G., Zhang, H., Wang, J., Xu, H. Accurate structural characterization of nanopores in coal by cryo-FIB-SEM. Advances in Geo-Energy Research, 2024, 14(3): 187-200.
https://doi.org/10.46690/ager.2024.12.04

Abstract:
The structural characteristics of nanopores are known to significantly affect the wetting effect in coal seam water injection. Currently, the three-dimensional characterization of nanopores in coal relies mainly on digital images, whereas poor image resolution and segmentation methods pose significant challenges. Therefore, using coal samples from Wudong Coal Mine in China as an example, cryo-focused ion beam scanning electron microscopy (cryo-FIB-SEM) and deep learning segmentation methods were implemented to accurately characterize the nanopores and water distribution. In the obtained pore structure, the number of isolated pores was higher than that of connected pores, while the volume of connected pores was significantly larger than that of isolated pores, comprising the key path and storage space for external water to enter the coal body. The water content of isolated pores mainly depends on the permeability of the coal matrix. The connectivity of single pores can be characterized by the coordination number, whose increase leads to the number of pores exponentially decreasing. The connectivity of pore clusters depends on the number of internal branches. The number of branches in the pore cluster increases exponentially with the increasing total length, total volume and average radius of the cluster, and the connectivity is correspondingly enhanced. The increase in pore size enhances the shape factor, surface area and connectivity of pores while reducing tortuosity, which in turn facilitates coal wetting. The accurate characterization of coal nanopores in this study helps to scientifically evaluate the effect of coal seam water injection, highlighting the importance of increased pore size and improved pore connectivity for enhanced water injection effectiveness.

1. Introduction

Coal seam water injection as a multifunctional mine disaster prevention measure achieves dust reduction and removal, gas control, anti-blowout and pressure relief, and coal and rock softening (Yang et al., 2020; Liu et al., 2021a; Wang et al., 2023). In this regard, pores and fractures are the main spaces for water seepage, and their development degree largely affects the wetting range and effect of coal seam water injection (Wang et al., 2022; Qin et al., 2023). Conventional reservoirs such as sandstone are characterized by micron-scale

Yandy Scientific Press

*Corresponding author.
E-mail address: gang.wang@sdust.edu.cn (G. Wang); chen0812zzzz@163.com (X. Chen); wanggang1110@gmail.com (G. Wang); 52zhq@163.com (H. Zhang); wjingsdu@163.com (J. Wang); xhaq866@163.com (H. Xu).

Received September 19, 2024; revised October 15, 2024; accepted November 7, 2024; available online November 12, 2024.

pores, while coal reservoirs are usually dominated by pores at the nanoscale (Jiao et al., 2014; Tang et al., 2016). The precise characterization of nanopores in coal seam is of great significance for the study of water seepage law in coal and the evaluation of the coal seam water injection effect.

During long-term geological evolution, nano- to microscale pores in coal form a tortuous, complex and highly heterogeneous pore network, where the pores become partially or completely connected. These inherent pore characteristics pose a major challenge to the comprehensive understanding of pore structure in coal seam. At present, pore structures in coal seam are mainly characterized by three techniques. The first one is microscopy imaging, such as by scanning electron microscopy (Li et al., 2024b), field emission scanning electron microscopy (Wang et al., 2020), focused ion beam scanning electron microscopy (FIB-SEM) (Zhou et al., 2024), transmission electron microscopy (Vranjes-Wessely et al., 2020), helium ion microscopy (Wu et al., 2020), atomic force microscopy (Li et al., 2024a), etc. This method presents the advantages of high magnification, excellent resolution, and the ability to provide high-quality images and strong 3D features, yet it is destructive and can generally observe pore/fracture structures only at the 2D level. The second group of methods are fluid injection analyses, including nuclear magnetic resonance (Zhou et al., 2023), mercury intrusion (Jiang et al., 2019), N_2/CO_2 adsorption (Mazumder et al., 2024), etc. Since any fluid needs to be injected into the test sample under a certain pressure, these methods tend to damage the pore structure and the observation range is limited by the fluid pressure. Besides, the results cannot visualize the pores but only indirectly reflect the characteristics of pore structures. The third set of methods are derived from X-ray spectroscopy, mainly including small-angle X-ray scattering (Sun et al., 2019), small-angle neutron scattering (Zhang et al., 2021) and computed tomography (Liu et al., 2021b). Such techniques are non-destructive, efficient and provide excellent visualization, thus have been widely used in the microstructure characterizations of coal samples.

Due to their varying working principles, different techniques can characterize pores of different size ranges. Unlike the fluid injection method, microscopy imaging and X-ray spectroscopy are visualization methods that can accurately image the morphology, connectivity and spatial distribution of pores and quantify their geometric structural characteristics. Among them, FIB-SEM tomography has more advantages in nanopore characterization (Li, 2018; Yu et al., 2024). For a typical FIB-SEM imaging process, the sample is sequentially ground with an ion beam in the perpendicular direction, and the newly exposed surface is imaged using an electron beam to generate a series of two-dimensional grayscale images, achieving the 3D reconstruction of nanopores inside the coal sample. In recent years, due to its high resolution, FIB-SEM has been widely used in the characterizations of various porous media, such as polymers (Röding, 2021), battery electrodes (Vierrath et al., 2015), oil and gas shales (Wu et al., 2020), sandstones (Jacob et al., 2021), and coal (Li et al., 2018; Li et al., 2023). However, FIB-SEM measurement requires dry samples. The structure of the water-containing sample may be altered during the drying process and thus cannot be accurately characterized (Liu et al., 2024). Nevertheless, the emergence of cryo-focused ion beam scanning electron microscopy (cryo-FIB-SEM) has addressed this issue. Cryo-FIB-SEM rapidly freezes the water in a water-containing sample into small and uniform ice crystals, without destroying its pore structures, and directly images its internal structure. It has showed significant advantages in the observation of water-containing samples, such as plant and animal tissues (Capua-Shenkar et al., 2022; Raguin et al., 2023), microorganisms (Jantschke et al., 2020), hydrated glass (De Winter et al., 2013), and soil (Lubelli et al., 2013).

The key to the accurate characterization of pores in coal by electron microscopy is the precise extraction thereof based on grayscale images. However, the cryo-FIB-SEM imaging of porous media tends to produce "pore back" artifacts, which makes the traditional threshold segmentation methods, such as interactive threshold segmentation, Otsu threshold segmentation, and watershed segmentation, no longer applicable (Saif et al., 2017; Zang et al., 2023). When a human expert looks at these images, their brain will take action to eliminate noises and artifacts and successfully identify the object region, yet it is difficult to achieve such a process through automation or calculation (Schlüter et al., 2014). The emergence of deep learning provides the possibility to realize this process without labor-intensive manual assessment. Deep learning obtains the features of the object region by the machine analysis of the manually segmented image. These features are then connected into a single "feature vector" and applied to the entire image to effectively segment the cryo-FIB-SEM image. Deep learning has been widely used in the image segmentation of pores in polymers (Čalkovský et al., 2021), battery electrodes (Bailey et al., 2023), shales (Andrew, 2018), and tight reservoir rocks (Kazak et al., 2021). It was found that the machine learning-based classification could better tolerate artifacts and noises than any traditional algorithm (Andrew, 2018).

Despite its remarkable advantages, previous studies have revealed two deficiencies of FIB-SEM in the characterization of coal nanopore structure:

1) The drying treatment before FIB-SEM imaging irreversibly changes the pore morphology, making it impossible to determine the water contents in the nanopores after water injection. Cryo-FIB-SEM technology can solve these problems, but it is rarely used in coal structure observation.
2) Traditional threshold segmentation methods are affected by "pore back" artifacts in the cryo-FIB-SEM image, which makes the characterization results inaccurate.

Therefore, this study attempted to scan the coal sample both in the original and the water-saturated state by cryo-FIB-SEM, and accurately segment the nanopores in the image with the assistance of deep learning, to reconstruct their 3D structure and analyze their structural characteristics. This approach provides a new idea for the observation of water in coal and a sound theoretical basis for improving the coal seam water injection effect at the microscopic level.

2. Materials and methods

Table 1. Industrial analysis of Wudong coal.

Coal rank	Industrial analysis (wt%)				Elemental analysis (wt%, daf)				
	Water	Ash	Volatile component	Fixed carbon	C	H	O	N	S
Lignite	6.27	12.02	30.19	51.52	74.50	4.93	18.71	0.99	0.87

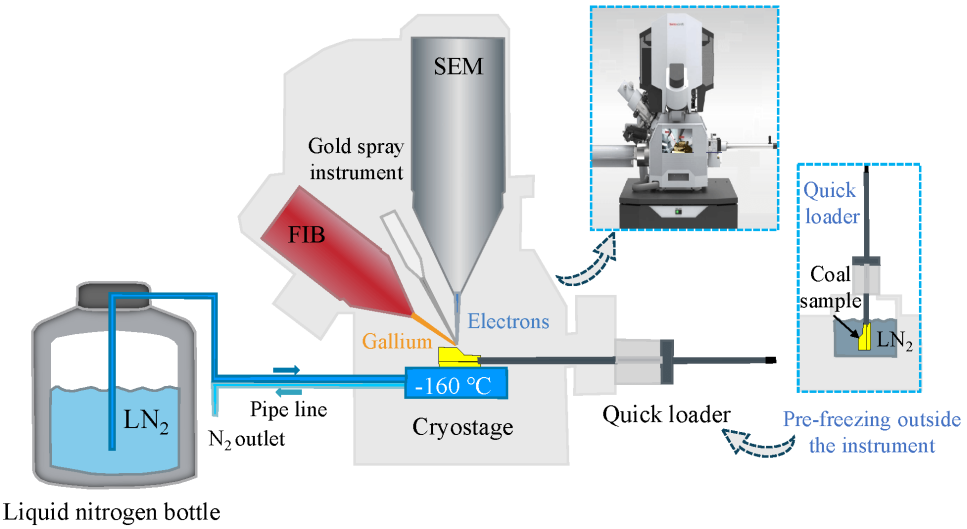

Fig. 1. Schematic diagram for the cryo-FIB-SEM scanning system.

2.1 Selection and preparation of coal sample

The coal sample used for this study was collected from the Wudong Coal Mine located in the southern margin of the Junggar Basin in China. The industrial analysis results of this coal are shown in Table 1. A relatively flat coal block was cut from the working face, carefully covered with plastic wrap and sent to the laboratory for further processing. Three rectangular coal samples with about 2 cm diameter, S1, S2 and S3, were cut from different positions of the same coal block and their surfaces were gently polished with fine sandpaper. S1 was immersed in water for 3 days to observe the distribution of water in coal, while S2 and S3 were not treated.

2.2 Cryo-FIB-SEM imaging

A Helios 5 CX dual beam electron microscope system (Thermo Fisher Scientific) consisting of an ion beam gun, an electron beam gun and a quick sample loader was used for cryo-FIB-SEM imaging (Fig. 1). Following the typical imaging process, the coal sample was first placed in the quick loader and pre-frozen with liquid nitrogen outside the instrument. When the water inside the coal sample was completely frozen, the sample with the quick loader was transferred to the Cryostage inside the instrument. Liquid nitrogen was continuously circulated to maintain a uniform freezing state at 160 °C. The coal sample was sprayed with a layer of gold in the sample chamber for good conductivity. The back-facing electronic module was then activated to enlarge the observation range, and a region of interest was selected on each coal sample. The angle between FIB and SEM guns was adjusted to 54° to ensure that the slicing was perpendicular to the surface of the region of interest before the slice scanning was started. Table 2 lists the scanning and imaging parameters.

2.3 Image preprocessing and deep learning segmentation

The images obtained with the cryo-FIB-SEM system were pre-processed as shown in Fig. 2 before undergoing segmentation. During imaging, the probe inevitably produced 2-3 nm shaking movements. Therefore, the images were first automatically aligned using the "Auto align slices" module of the Avizo platform. Because of the inconsistences in slice thicknesses and imaging size (Table 2), the images were blurrier in the z direction than the x and y directions. To solve this problem, the resolution of the image z axis was increased to 50 nm by activating the "Resample" module. In addition, there were irregular edges without pores and fractures around the coal sample in the images, affecting the observation. To eliminate this problem, the effective areas containing pores in the image were manually divided, and the boundaries of the effective regions were generated by semi-automatic watershed segmentation. Finally, the invalid areas in the images were hidden using the "mask" module and the images were denoised using the median filter, which could effectively remove salt and pepper noise (Zhao et al., 2018).

The deep learning image segmentation was conducted using the segmentation wizard of the Avizo platform "Deep Learning Interface (Python 3.6.13)", with the following steps:

1) Select part of images from the preprocessed images as

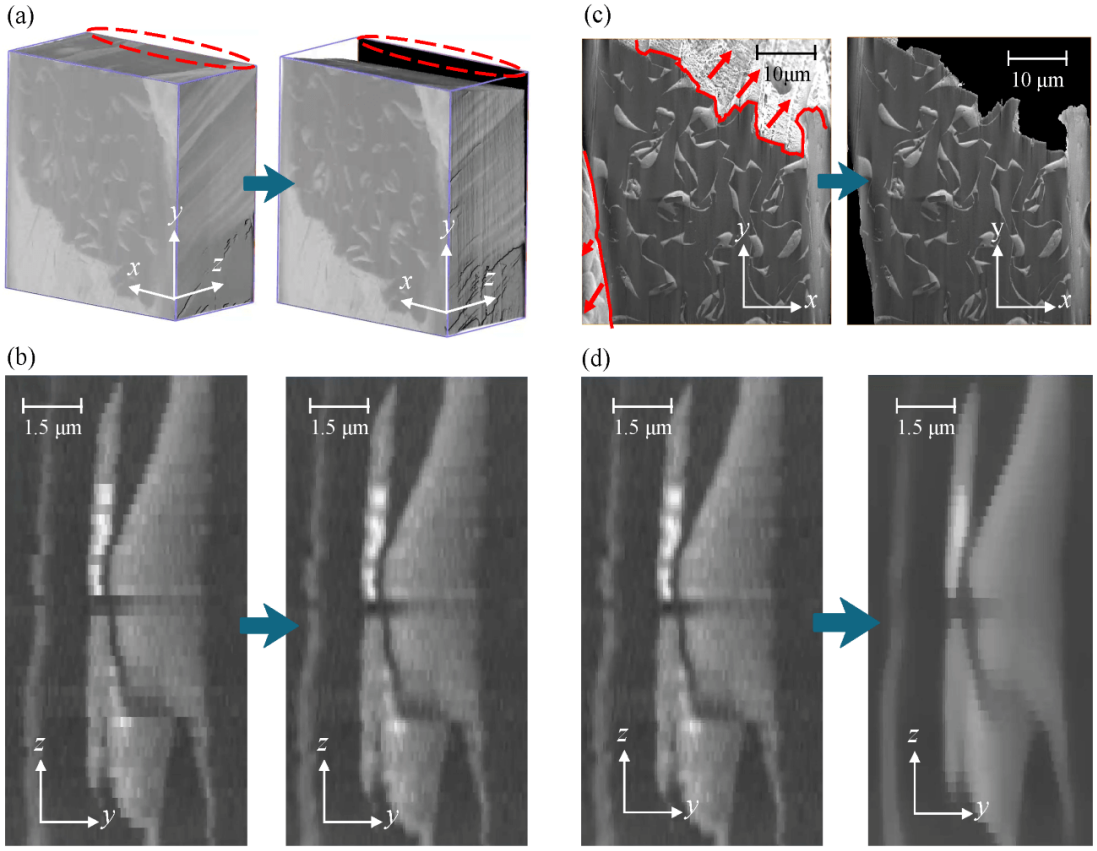

Fig. 2. Image pre-processing: (a) Automatic image alignment, (b) improved *z*-direction resolution, (c) effective region extraction and (d) noise reduction.

Table 2. Scanning and imaging parameters for three coal samples.

Sample	SEM voltage (kV)	Electron beam current (nA)	Slice thickness (nm)	Image resolution (nm)	Number of images
S1	2	0.4	180	50 × 50	149
S2	2	0.4	180	50 × 50	450
S3	2	0.4	180	50 × 50	491

the training set;

2) Roughly divide the object region (pores and fractures in S2 and S3 and water in S1) using interactive threshold segmentation. Note that the extracted areas must be smaller than the actual object region;
3) Manually segment the subtle object regions not segmented perfectly in the previous step;
4) Generate a deep learning model using the segmented image;
5) Extract the object regions from the original images using the deep learning model.

In Step 1), to comprehensively obtain the features of the image, slices were selected as the training set through uniform intervals. Among them, 10, 22, and 24 slices were selected for S1-S3 as their training sets, respectively.

The training accuracy of the three samples reached more than 90%. In addition, the Avizo platform provides a secondary deep learning module. To further accurately extract the target areas, the areas of unsatisfactory segmentation were re-segmented manually in the module. Then, a portion of the area with a size of 64×64 Pixel^2 was selected after calibration as the model for secondary deep learning. Among them, the number of selected regions was determined based on the size of the correction region. Ten regions were selected for S1, while 20 regions were selected for S2 and S3, which improved the model accuracy to more than 95%.

2.4 Construction of centerline model

Fig. 3(a) shows the reconstructed 3D pore model, which could effectively reflect the spatial distribution and morphological characteristics of pores. However, coal is a heterogeneous rock with a highly complex and irregular pore network, which is inconvenient for subsequent topological connectivity characterization and quantitative analysis. To solve this problem,

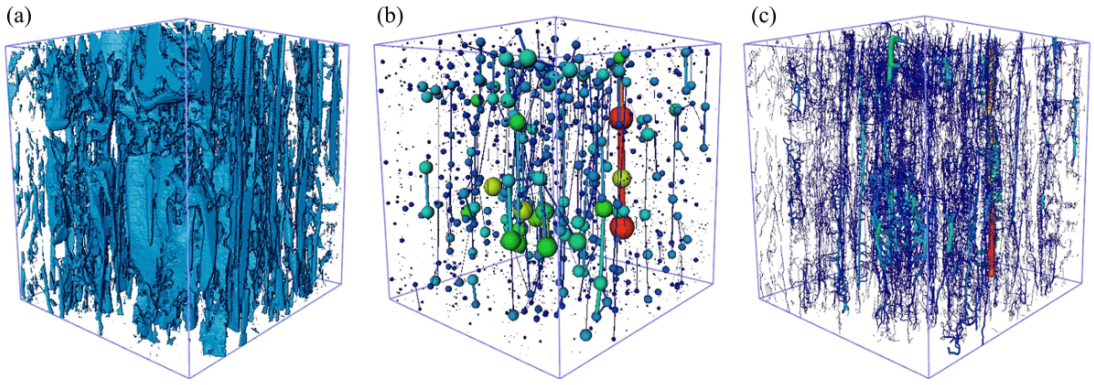

Fig. 3. 3D pore model and the simplified models: (a) 3D pore and fracture model, (b) ball-and-stick model and (c) centerline model.

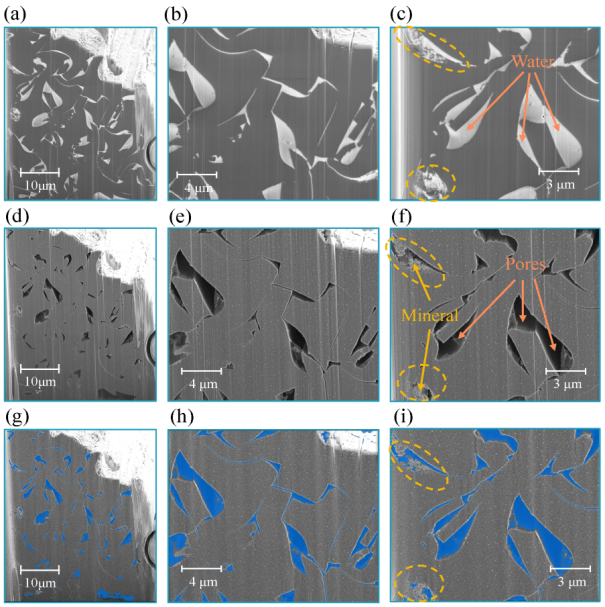

Fig. 4. Cryo-FIB-SEM images at (a)-(c) 160 °C, (d)-(f) 25 °C and (g)-(i) at the same positions and water segmentation of S1.

an equivalent simplified structural model is needed that reflects the topological structure of the pores. At present, the most common simplified model to characterize the pore network in coal is the ball-and-stick model. As shown in Fig. 3(b), pores are equivalent to spheres of equal volumes and throats are equivalent to sticks of equal diameter. Thus, the model intuitively reflects the connectivity between pores and can be used to further calculate the properties of the network. On the other hand, this network model has certain defects. First, simplifying the throats connecting the pores to a straight line ignores the curvature (tortuosity) of the throats. Second, fractures are equivalent to spheres in the model, which is quite different from their actual shapes.

To overcome these defects, we constructed a centerline model as shown in Fig. 3(c). On the basis of the "Auto Skeleton" module of the Avizo platform, the main morphologies and topologies of the pores were kept unchanged, and the remaining topological skeleton structure was gradually extracted by continuously removing the outer morphological pixels of the pores while the spatial connectivity and geometric characteristics of the pore microstructure was maintained to the greatest possible extent. The model was further divided into different groups based on the connectivity degrees of the pores. Unlike the ball-and-stick model, the centerline model can reflect not only the connectivity between the pores but also the pore directions. Thus, tortuosity can be further calculated with the model.

3. Results

3.1 Water distribution in a water-saturated coal sample

Fig. 4(a) and its zoomed-in views Figs. 4(b) and 4(c) depict the Cryo-FIM-SEM image of the water-saturated S1 sample obtained in the frozen state. To locate the water in the image, the temperature in the sample chamber was raised from -160 °C to 25 °C in order to evaporate the water and fully expose the pores. This process took about an hour to complete. The sample was then re-scanned and images were collected at the same position as those at low temperature. The black areas in Figs. 4(d)-4(f) for the images taken at room temperature were identified as pores. The comparison of the images obtained at low temperature and room temperature infers that the white areas in the Figs. 4(a)-4(c) are water. Qin and Zhang (2000) reported that the minimum pore size for water penetration and storage in coal was 70-220 nm. In this study, the smallest pore of S1 was measured to be about 520 nm in diameter, larger than the threshold pore size for water penetration. The images also show that almost all pores are filled with water.

It is worth noting that there are small amounts of white minerals detected in the coal sample, which manifest as white regions (yellow circles in Fig. 4(f)). The minerals together with water show larger and brighter regions at the same positions in the low temperature image (yellow circles in Fig. 4(c)), indicating that there is more water around the minerals and they are hydrophilic. The white areas with minerals in the low temperature images were removed by deep learning, as shown in Figs. 4(g)-4(i). It can be seen that the white areas in Figs. 5(a)-5(c) are all classified as water but not the mineral

areas

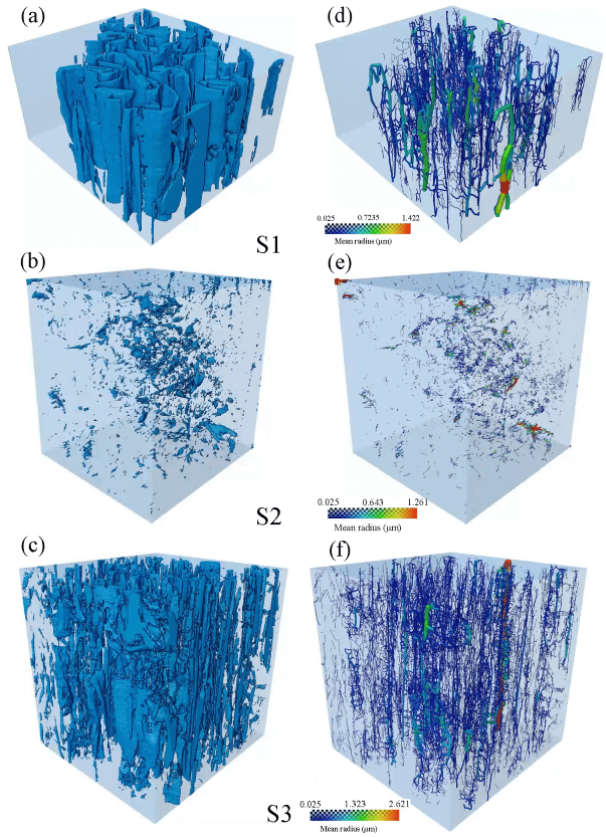

Fig. 5. (a)-(c) Spatial distributions of pores/fractures in S1, S2 and S3 and (d)-(f) their centerline models.

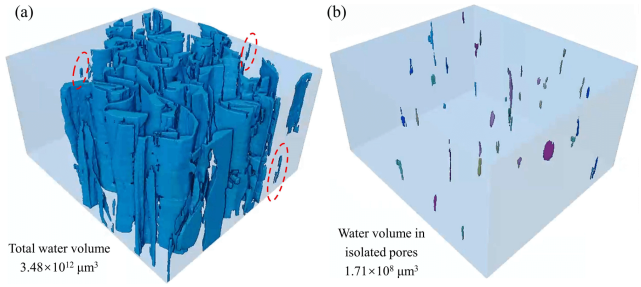

Fig. 6. 3D water distribution in coal: (a) Water in pores and (b) water in isolated pores.

in Figs. 5(d)-5(f), which further demonstrates the accuracy of deep learning segmentation. The 3D distribution of water in the coal sample was obtained by image reconstruction as shown in Fig. 6. The total volume of the scanning area of S1 is 4.13×10^{13} μm^3, where the water volume was determined to be 3.48×10^{12} μm^3. The water distribution is relatively continuous, indicating that water enters the coal sample mainly through connected pores. It was reported that water could not enter isolated pores (Guan et al., 2023; Zhang et al., 2023). However, scattered water distribution areas were observed in S1, that are neither connected to other water-containing areas inside the coal nor are in contact with external water (red circles in Fig. 6(a)), indicating that water can enter isolated

Table 3. Heterogeneity of the parameters of three coal samples.

Parameters		S1	S2	S3
Porosity (%)	Pores	3.44	45.83	24.32
	Fractures	96.56	54.17	75.68
Direction proportion (%)	0° ~ 30°	73.85	7.89	96.71
	30° ~ 60°	0	42.62	3.29
	60° ~ 90°	26.15	49.50	0
Volume proportion (%)	Connected pores	88.66	34.79	79.51
	Isolated pores	11.34	65.21	20.49
Number proportion (%)	Connected pores	47.3	1.28	4.16
	Isolated pores	52.7	98.72	95.84

pores in coal by penetrating through the coal matrix with high permeability. Fig. 6(b) illustrates these isolated pores extracted from the image. Their total volume was calculated to be 1.71×10^8 μm^3, accounting for only 0.0049% of the total water volume in the coal sample. These results suggest that water mainly enters into coal through connected pores and to a small extent through the coal matrix.

Overall, connected pores are the key transportation path and storage space of water and play a decisive role in increasing the water content of coal seam during water injection. The water content in isolated pores mainly depends on the permeability of the coal matrix. For the coal dominated by isolated pores, high permeability is particularly critical to achieve better water injection effects. In addition, the presence of hydrophilic mineral components can also increase the water content in coal to a certain extent.

3.2 3D distribution and heterogeneity of pores

Since almost all pores in S1 are filled with water, the water distribution in this sample is used to characterize the development of its pores. Fig. 5 presents the spatial distributions of pores and their centerline models in the three samples, which reveals significant differences in their pore shapes, volumes, connectivity, and high heterogeneity. S1 and S3 exhibit large pore volumes and their fractures are mostly slender and highly connected with each other, which are conducive features to the entry and seepage of water. In contrast, the pore volume of S2 is small and there are more isolated pores, allowing water to enter mainly through the coal matrix. The detailed differences between coal samples in the proportions of pores and fractures, the numbers of connected pores, and the pore volumes are presented in Table 3.

The pores and fractures in coal can be distinguished on the basis of the shape factor H as shown in Eq. (1). If $H = 1$, the pore is a standard sphere. The larger the shape factor is, the longer the pore and the closer it is to a fracture. Taking the pores in S3 as an example, their shape is closer to a pore when $H < 30$ and closer to a fracture when $H > 30$ (Fig. 7).

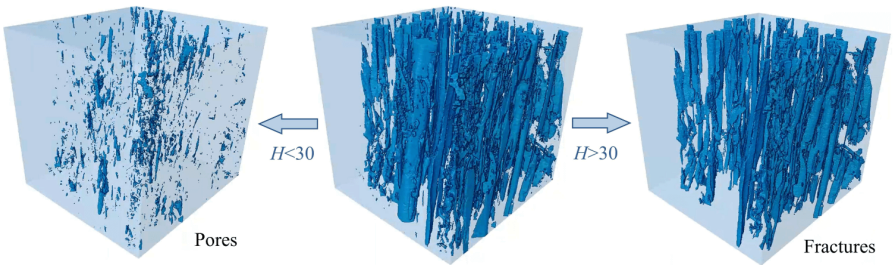

Fig. 7. Classification of pores and fractures in S3.

Table 4. Structure parameters of three coal samples.

Sample	Number of pores/fractures	Porosity (%)	Fractal dimension	Shape factor
S1	88	8.42	2.19	43.95
S2	2,765	0.24	1.74	7.50
S3	3,811	5.88	2.20	31.05

Therefore, the pores and fractures in all three coal samples were distinguished using $H = 30$ as the boundary, and their volumes were calculated. As shown in Table 3, for all three samples, the total volumes of fractures are greater than those of pores. In particular, fractures contribute by 96.56% to the porosity of S1, suggesting that it is a typical fracture-type coal. The proportion of fractures in S3 is also high at 75.68%. The pore volume and fracture volume of S2 are similar, accounting for 45.83% and 54.17% of the total pore volume, respectively:

$$H = \frac{A^3}{36\pi V^2} \tag{1}$$

where H, A and V respectively represent the shape factor, specific surface area and volume of the pore/fracture.

In contrast to pores, fractures in coal are directional, and their direction is the main controlling factor of coal permeability, failure mode and other characteristics (Wang and Teng, 2022; Zhou et al., 2022). Table 3 lists the volume proportions of fractures with different directions that are expressed with the angles with the z direction. As can be seen in the figure, the fractures in S1 and S3 are strongly directional, mostly parallel to the z-axis. The volume proportions of fractures with the angles of 0°-30° are 73.85% and 96.71% in S1 and S3, respectively, and more than 90% of fractures are at angles smaller than 60°. Therefore, water injection from different directions face significantly varying difficulty. For instance, that in the z direction allows water to rapidly enter the coal body along the connected fractures and this results in high water injection rates. Injecting water from other directions is more difficult as water needs to pass through the coal matrix and a small number of connected fractures in other directions, leading to low water injection rates. The water injection effects in different directions may eventually become similar if sufficient time has passed, yet the water injection rates in other directions will be much lower than that in the z direction due to the need to penetrate the coal matrix. In contrast, the inclination angles of fractures in S2 are larger, with more than 90% of them being greater than 30°, and only 7.89% of fractures parallel to the z-axis.

Table 3 presents the connectivity of pores/fractures in the samples. Apparently, the numbers of connected pores/fractures in S1-S3 are lower than the numbers of isolated pores/fractures, accounting for only 47.30%, 1.28% and 4.16% of the corresponding total numbers of pores/fractures, but contributing 88.66%, 34.79% and 79.51% of their total pore volumes, respectively. In particular, the volumes of the connected pores in S1 and S3 are 77.32% and 59.02% higher, respectively, than those of isolated pores. Although the number of connected pores in S2 is 98.72% lower than that of isolated pores, their total volume is only 30.42% lower. These results suggest that the volume of a connected pore is significantly larger than that of an isolated pore. The presence of connected pores/fractures is conducive to water injection, and the larger volumes of these pores/fractures also provide sufficient water storage spaces, which is of great significance for improving the coal seam water injection effect.

3.3 Pore size distribution

Table 4 lists the comprehensive structure properties of pores/fractures in S1, S2 and S3, including porosity, number of pores/fractures, average shape factor, and fractal dimension. Sample S1 contains only 88 pores/fractures yet shows the highest porosity of 8.42% because the volume of each pore/fracture in S1 is large (Fig. 5(a)). There are 2,677 more pores in S2 than S1, but its porosity is only 2.85% of that of S1 because its pores/fractures are much smaller. The number of the pores/fractures is the largest in sample S3 with the value of 3,811, and its porosity is 5.88%, second to that of S1. Fractal dimension can quantitatively characterize the complexity of a porous structure. In general, the larger the fractal dimension is, the more complex the pore/fracture network (Wang et al., 2019; Zhang, 2024). The fractal dimensions of S1 and S3 are similar, exhibiting values of 2.19 and 2.20, respectively. Theoretically, the fractal dimension of the 3D model of a pore/fracture network ranges from 2 to 3 and it is only lower than 2 if the pore network is extremely simple (Wang et al., 2024). The fractal dimension of S2 sample is 1.74, suggesting that its pore/fracture structure is simple and cannot generate a complex porous network as indicated by the porosity. The average shape factors of S1 and S3 are 43.95 and 31.05, respectively, both higher than the criterion of 30 to distinct pores and fractures, indicating that their porous structures are dominated by fractures. The average shape factor

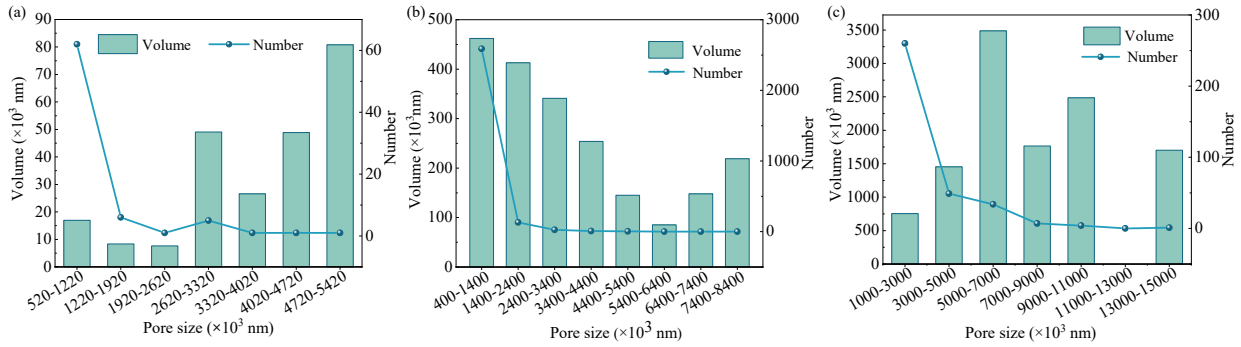

Fig. 8. Volume and size distributions of pores/fractures in samples (a) S1, (b) S2 and (c) S3.

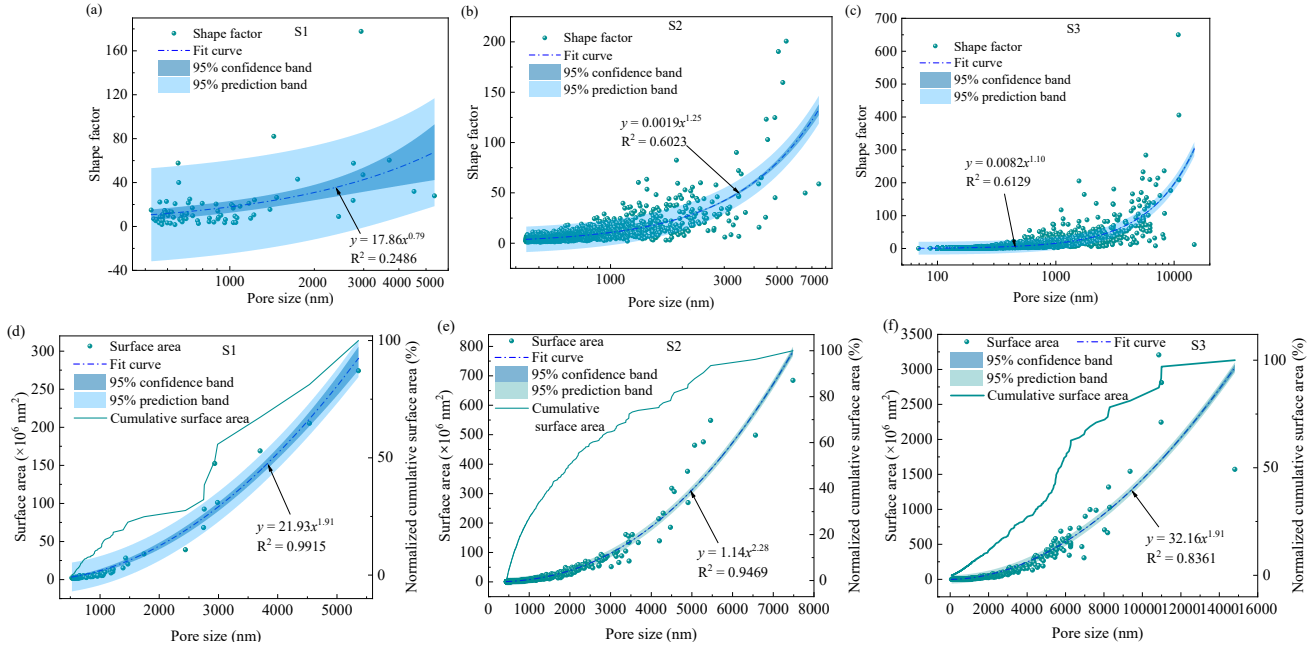

Fig. 9. (a)-(c) Shape factor and (d)-(f) surface area distributions under different pore size ranges.

of S2 is 7.50, confirming that this sample mainly contains pores.

To explore the correlation between the structural properties and size of pore/fracture, the distributions of pore number, volume, surface area, and shape factor in different pore size ranges were further analyzed. As shown in Fig. 8, the number of pores/fractures first decreases dramatically and then becomes constant in all three samples with increasing pore size. Specifically, as the pore size increases from the first to the second stage, the pore numbers of S1, S2 and S3 samples decrease by 90.32%, 94.94% and 81.15%, respectively. The pore volume distribution is relatively dispersed, showing no obvious change pattern with the pore size. The peak pore volume of S1 is found in the pore size range of 4.72×10^6-5.42×10^6 nm. There are only 7 fractures in this size range, but they contribute by nearly 40% to the total pore volume. The number of pores/fractures in the size range of 5.2×10^5-1.22×10^6 nm is the largest, while their total volume is relatively small. The pore volume of S2 sample peaks in the pore size range of 4×10^5-1.4×10^6 nm, which contains the largest number of pores/fractures and gradually decreases as the pore size increases. As the pore size reaches 5.4×10^6-6.4×10^6 nm, the pore volume increases again, attributed to the increases in the volumes of single large pores. The peak pore volume of S3 is found in the pore size range of 5×10^6-7×10^6 nm, and the pore volumes in other pore size ranges are similar.

The shape factor exhibits an exponential relationship with the pore size (Figs. 9(a)-9(c)). Fitting in the 95% confidence interval reveals strong correlations between shape factor and pore size of $y = 0.0019x^{1.25}$ and $y = 0.0082x^{1.10}$ in S2 and S3, respectively. The correlation is not obvious in the S1 sample due to its small number of pores/fractures. Combined with the definition of shape factor described above, the exponential relationship between shape factor and pore size can be understood as follows: The larger the pore size is, the greater the possibility of the pore to propagate outward and the greater the corresponding shape factor. The pore surface area and pore size show more obvious exponential correlations, with the equations of $y = 21.93x^{1.91}$, $y = 1.14x^{2.28}$ and $y = 32.16x^{1.91}$ in

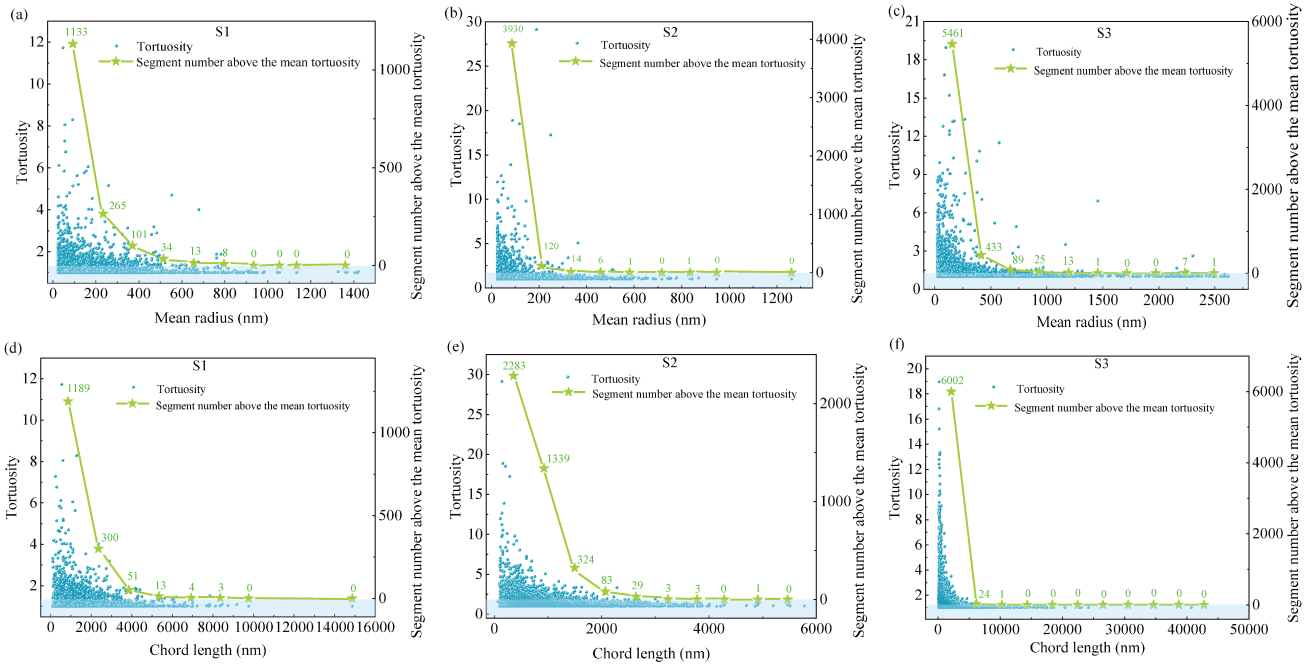

Fig. 10. (a)-(c) Relationships between average radius and (d)-(f) chord length with tortuosity.

S1, S2, and S3, respectively (Figs. 9(d)-9(e)). The cumulative surface areas of S1 and S3 show gradient growth patterns with increasing pore size, yet the increasing trend of S3 tends to slow down. That of S1 still maintains a high growth rate until reaching 70% before slowing down.

In our previous study, we have demonstrated that the shape factor of coal pore/fracture is positively correlated with the water seepage velocity during coal seam water injection, and the larger the pores/fractures is, the stronger their connectivity (Wang et al., 2022). In addition, larger pore surface areas can facilitate water infiltration through the coal body. Therefore, although the number of the large pores/fractures is small, their high connectivity, great extension lengths, and large surface areas can significantly improve the coal seam water injection effect.

3.4 Pore/fracture tortuosity characteristics

Tortuosity reflects the degree of curvature of pores/fractures in coal. The greater the tortuosity is, the more complex the water transportation path and the more difficult the water injection becomes. Taking the actual arc length of a fracture as l, and its chord length as l_s, its tortuosity T is the ratio of l to l_s, as shown in Eq. (2) (Guo et al., 2021). The greater the tortuosity is, the curlier the fracture. Since the centerline model retains the shape characteristics of the fracture, the Avizo platform can be utilized to accurately calculate the tortuosity of each fracture:

$$T = \frac{l}{l_s} \tag{2}$$

According to the center of fracture direction, the constructed centerline model is an equivalent tubular model. Each equivalent tubular pore/fracture is called a "branch", and the radius of a branch is different at different positions. For the convenience of analysis, the average radius is introduced to represent the radius of a branch, which can be expressed as:

$$r = \sqrt{\frac{V_s}{\pi l}} \tag{3}$$

where r represents the average branch radius and V_s is the volume of the branch.

Figs. 10(a)-10(c) show the tortuosity of pores/fractures with different average radii in S1-S3. The average pore/fracture tortuosity of S1, S2 and S3 are 1.2008, 1.3262 and 1.1727, respectively. The low tortuosity pores/fractures are evenly distributed in each radius range, but those with high tortuosity are mostly concentrated in the low average radius range. To intuitively show this phenomenon, the numbers of pores/fractures with greater-than-average tortuosity in different radius ranges in Figs. 10(a)-10(c) were counted. It was found that, with increasing average radius, the number of pores with greater-than-average tortuosity gradually decreases and eventually approaches 0. Combined with the previous analysis, these results suggest that the volumes, shape factors, and surface areas of the pores/fractures with smaller radii are all small, while their curvatures are large, which causes poor water permeability. As shown in Figs. 10(d)-10(f), the changing trend of tortuosity with chord length is similar to that with average radius. The low-tortuosity pores/fractures are more concentrated in the low chord length ranges. Similarly, the number of pores/fractures with greater-than-average tortuosity decreases rapidly with increasing chord length in all samples. In particular, as the chord length increases to above 10,000 nm in S3, there are no pores/fractures with greater-than-average tortuosity.

3.5 Pore/fracture connectivity characteristics

As demonstrated in Section 3.1, connected pores/fractures contribute to most of the water storage space in coal and are an important indicator for evaluating the seepage capacity of the

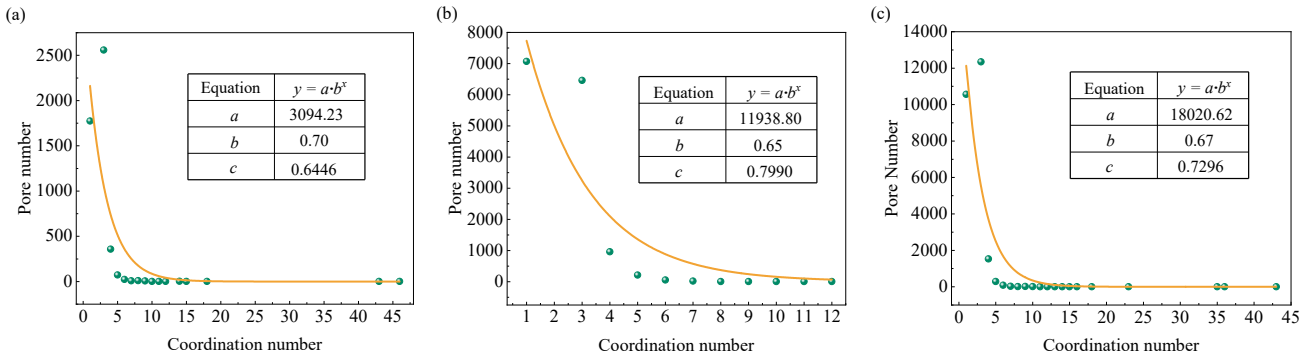

Fig. 11. Numbers of pores/fractures with different coordination numbers in (a) S1, (b) S2 (b) and (c) S3.

porous matrix (Liu et al., 2020). The structural characteristics of connected pores/fracture will be further discussed in this section. The centerline model is composed of many isolated pore/fracture clusters, and each cluster is composed of multiple interconnected pores and fractures (branches) (Figs. 5(d)-5(f)). Therefore, based on the centerline model, this section explores the pore/fracture connectivity at two levels: Single pore/fracture and pore/fracture cluster.

3.5.1 Pore/fracture connectivity

For an individual pore/fracture, its connectivity can be evaluated by the coordination number, defined as the number of throats connecting a pore/fracture to other pores/fractures. The coordination number of an isolated pore/fracture is 0. As demonstrated in Table 3, the number of isolated pores/fractures is significantly larger than that of connected pores/fractures. To further explore the relationship between the connectivity and number distribution of pores/fractures, connected pores/fractures in the model were extracted and the numbers of pores/fractures with different coordination numbers were counted. It was found that the number of pores/fractures shows similar exponentially decreasing trends with increasing coordination number in the three samples (Fig. 11). Since S1 and S3 mainly contain fractures with larger propagation lengths, and the possibilities for them to connect with other pores/fractures are higher, the number of pores/fractures with larger coordination numbers in S1 and S3 is larger than that in S2.

3.5.2 Connectivity of pore/fracture cluster

The connectivity of a pore/fracture cluster depends on the number of internal pores/fractures, i.e., its branches. According to the author's previous research (Wang et al., 2022), the connectivity of a single pore/fracture is affected by its propagation length. The larger the propagation length is, the stronger the connectivity. To determine whether this correlation also exists in pore/fracture clusters, the relationship between the total length of all branches and the number of branches was statistically analyzed. The results revealed a strong exponential relationship between the number of branches in a cluster and their total length with the correlation coefficients over 95% for all three samples (Figs. 12(a)-12(c)). Therefore, pore/fracture length is considered a key factor affecting the connectivity of either an individual pore/fracture or a pore/fracture cluster. The larger the length is, the stronger the connectivity.

In addition to length, the number of branches in a pore/fracture cluster is also correlated to its total pore volume and average radius. The average radius of a pore/fracture cluster can be calculated according to:

$$R = \sqrt{\frac{V_1 + V_2 + \cdots + V_n}{\pi L}} \tag{4}$$

where R represents the average radius of the pore/fracture cluster, $V_1, V_2, \cdots, V_n$ denote the branch volumes in the cluster, and L is total pore/fracture length of the cluster.

Similar to the total length, the total volume of pore/fracture cluster exponentially increases with the number of branches (Figs. 12(d)-12(f)). The larger the volume of the cluster is, the stronger its connectivity. However, this correlation is significantly weaker than that between total length and branch number; especially, the correlation coefficient in S2 and S3 are only 0.4604 and 0.1658. The average radius of the pore/fracture cluster is quadratically related to the number of branches in S1 and S3, but this correlation is weak (Figs. 12(g)-12(i)). No obvious correlation was found between the average radius and the number of branches in S2.

The pore/fracture clusters with the strongest connectivity were extracted from each of the samples for comparison (Fig. 12). It was found that the larger the total length, the total volume and the average radius of the pore/fracture cluster is, the stronger its connectivity. The correlation between the number of branches and the total length, total volume and average radius of the pore/fracture cluster was stronger in S1 and S3 samples compared to S2, possibly because the former two are fracture-dominated coal samples with well-developed pore/fracture networks.

4. Discussion

The coal seam water injection process can be divided into two stages, i.e., seepage stage and wetting stage, as shown in Fig. 13. In the early water injection stage, the water injection rate mainly depends on the seepage velocity in large fractures. Later, the dominant mechanism shifts to matrix wetting, and the water diffusion mainly occurs in the micro/nanopores of the matrix. Insufficient wetting and serious water leaking can cause a poor field water injection effect, despite the

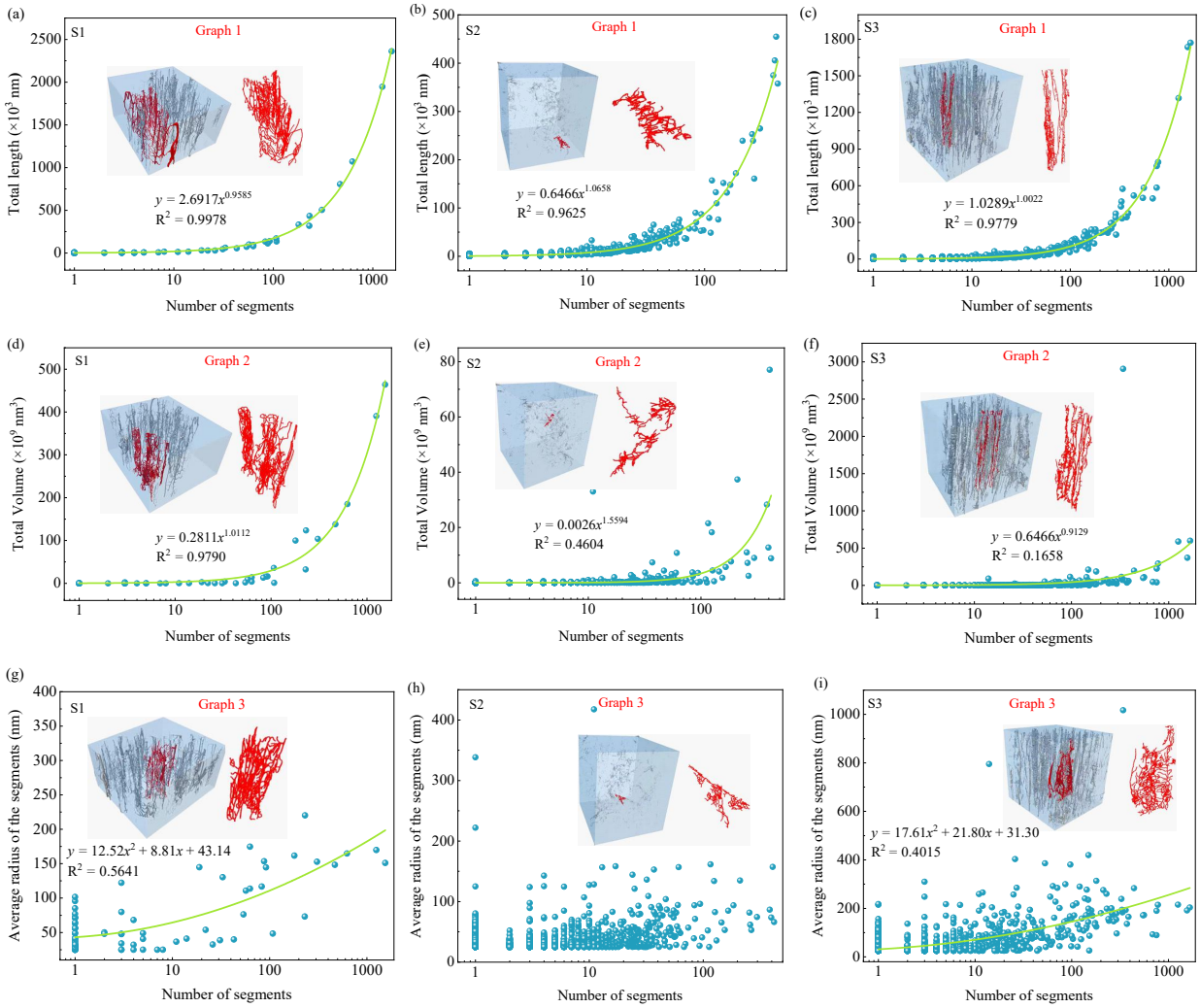

Fig. 12. Relationships between number of branches in a pore/fracture cluster and their (a)-(c) total length, (d)-(f) total volume and (g)-(i) average radius.

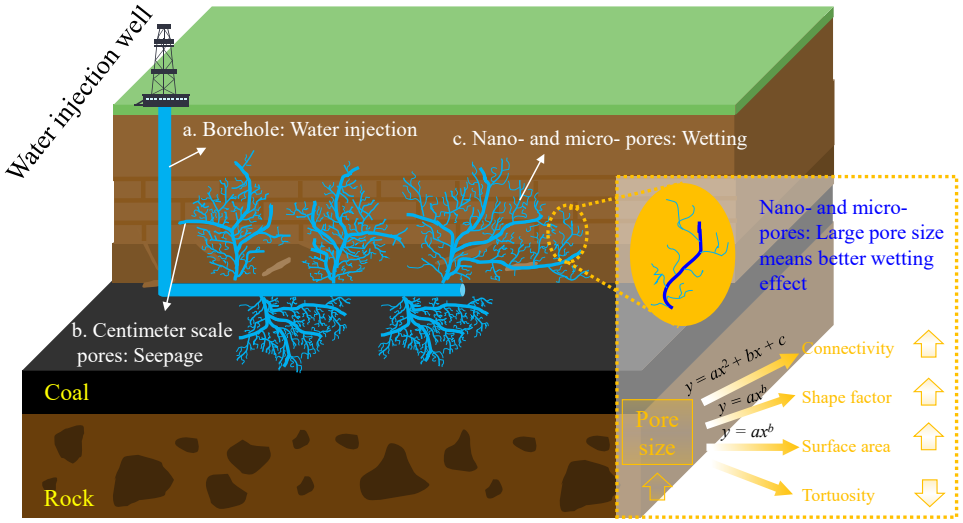

Fig. 13. The water injection process.

large amount of water injected (Zheng, 2022). Therefore, compared with the rapid seepage stage, the wetting stage plays a more decisive role in achieving good water injection effect via changing the physical and chemical properties of the coal seam and reducing dust production. The connectivity between pores/fractures is crucial to the wetting process. However, coal seams usually contain large numbers of isolated pores disconnected from the water injection pores/fractures. For example, the volume of isolated pores/fractures in S2 accounts for more than 50% of the total pore volume, and these pores/fractures can only obtain a small amount of water through matrix infiltration. Therefore, improving the connectivity of pores/fractures is the key to increasing the wetting range of water injection.

The statistical analysis reveals strong correlations between the size and multiple structural parameters of the pore/fracture. Pore size is positively correlated with shape factor, surface area and connectivity, while it is negatively correlated with fracture tortuosity (Fig. 13). From this point of view, the relationship between pore size and connectivity can be described as follows: the larger the pore is, the larger its shape factor and surface area. Larger pores/fractures are more likely to propagate in other directions and connect with other pores/fractures. In addition, they usually show lower tortuosity and seepage barriers, which is conducive to the wetting process. Therefore, pore size is a key structural parameter for the wetting process in the later stage of water injection. However, the number of large pores/fractures is small and their volume is not dominant (Fig. 8). To improve the water injection effect, attention should be paid to increasing the pore size and thus enhancing the connectivity of the pore/fracture network.

5. Conclusions

To better understand the properties of the nanopores including pore size distribution, tortuosity and connectivity in coal, we have determined and calculated the 3D distributions of water and pores/fractures and established a centerline model by cryo-FIB-SEM tomography and deep learning-based image segmentation. The findings are of great significance for improving the coal seam water injection effect. The main conclusions can be summarized as follows:

1) Connected pores comprise the key water transportation path and storage space for coal seam water injection. The water content in isolated pores mainly depends on the permeability of the coal matrix. The presence of hydrophilic minerals can increase the water content in coal to a certain extent.
2) The shape factor can be a used as a criterion to distinguish pore and fracture. Specifically, it is a pore when $H < 30$ and a fracture when $H > 30$. The fractures in S1 and S3 samples are highly directional. The volume proportions of their fractures with the angles of $< 30^\circ$ with the z direction are 73.85% and 96.71% respectively, and the angles of more than 90% of fractures are smaller than 60°. There are large numbers of isolated pores/fractures in the samples, but their volume is much smaller than that of the connected pores/fractures. The number of connected pores/fractures accounts for only 47.30%, 1.28% and 4.16% of the total pore number in S1, S2 and S3 samples, but they contribute 88.66%, 34.79% and 79.51%, respectively, of the total pore volumes of the corresponding samples.
3) The connectivity of pores/fractures are investigated from the prospects of single pore/fracture connectivity and pore/fracture cluster connectivity. The characterization of the connectivity of single pores/fractures with coordination number suggests that the number of pores/fractures gradually decreases with increasing coordination number. The connectivity of a pore/fracture cluster depends on the number of its internal branches. The porosity, total propagation length, total volume, and average radius of porosity exponentially increase with the increase in the number of branches, and the connectivity correspondingly becomes stronger.
4) Increasing the size and connectivity of pores is of great significance for improving the wetting effect of coal seam water injection. The shape factor and surface area become larger as the pore size increases, and thus larger pores/fractures are more likely to propagate in other directions and connect with other pores/fractures. Larger pores/fractures usually exhibit low tortuosity and cause little obstruction to seepage, which is conducive to the wetting of coal seam.

Acknowledgements

This work was supported by the National Natural Science Foundation of China (Nos. 52174194, 52274145 and 52404227).

Conflict of interest

The authors declare no competing interest.

References

Andrew, M. A quantified study of segmentation techniques on synthetic geological XRM and FIB-SEM images. Computational Geosciences, 2018, 22(6): 1503-1512.

Bailey, J. J., Wade, A., Boyce, A. M., et, al. Quantitative assessment of machine-learning segmentation of battery electrode materials for active material quantification. Journal of Power Sources, 2023, 557: 232503.

Čalkovský, M., Müller, E., Meffert, M., et, al. Comparison of segmentation algorithms for FIB-SEM tomography of porous polymers: Importance of image contrast for machine learning segmentation. Materials Characterization, 2021, 171: 110806.

Capua-Shenkar, J., Varsano, N., Itzhak, N. -R., et, al. Examining atherosclerotic lesions in three dimensions at the nanometer scale with cryo-FIB-SEM. Proceedings of the National Academy of Sciences of the United States of America, 2022, 119(34): e2205475119.

De Winter, M., Mesman, R. J., Hayles, M. F., et, al. Ion beam preparation and transmission-SEM imaging of frozen-hydrated, vitreous lamellas prepared by the Cryo-FIB-SEM: An all-in-one instrument. Microscopy and Microanalysis, 2013, 19(S2): 878-879.

Guan, X., Liu, Y., Ren, C., et, al. Characterization and comparison of pore structure and connectivity of anthracite based on CT three-dimensional reconstruction. Unconventional Oil & Gas, 2023, 10(1): 69-76. (in Chinese)

Guo, Y., Zhang, T., Du, J., et, al. Evaluating the chloride diffusion coefficient of cement mortars based on the tortuosity of pore structurally-designed cement pastes. Microporous and Mesoporous Materials, 2021, 317: 111018.

Jacob, A., Peltz, M., Hale, S., et, al. Simulating permeability reduction by clay mineral nanopores in a tight sandstone by combining computer X-ray microtomography and focussed ion beam scanning electron microscopy imaging. Solid Earth, 2021, 12(1): 1-14.

Jantschke, A., Pinkas, I., Schertel, A., et, al. Biomineralization pathways in calcifying dinoflagellates: Uptake, storage in MgCaP-rich bodies and formation of the shell. Acta Biomaterialia, 2020, 102: 427-439.

Jiang, J., Yang, W., Cheng, Y., et, al. Pore structure characterization of coal particles via MIP, N_2 and CO_2 adsorption: Effect of coalification on nanopores evolution. Powder Technology, 2019, 354: 136-48.

Jiao, K., Yao, S., Liu, C., et, al. The characterization and quantitative analysis of nanopores in unconventional gas reservoirs utilizing FESEM-FIB and image processing: An example from the lower Silurian Longmaxi Shale, upper Yangtze region, China. International Journal of Coal Geology, 2014, 128-129: 1-11.

Kazak, A., Simonov, K., Kulikov, V. Machine-learning-assisted segmentation of focused ion beam-scanning electron microscopy images with artifacts for improved void-space characterization of tight reservoir rocks. SPE Journal 2021, 26(4): 1739-1758.

Li, H., Cao, J., Lu, J., et, al. Effect of microwave-assisted cyclic oxidation on the coal internal and surface structure based on NMR and AFM. Energy, 2024a, 288: 129872.

Li, K., Tian, H., Liang, Y., et, al. The molecular model of organic matter in coal-measure shale: Structure construction and evaluation based on experimental characterization. Molecules, 2023, 28(13): 5203.

Li, L., Zhang, D., Su, Y., et al. Microfluidic insights into CO_2 sequestration and enhanced oil recovery in laminated shale reservoirs: Post-fracturing interface dynamics and micro-scale mechanisms. Advances in Geo-Energy Research, 2024b, 13(3): 203-217.

Liu, H., Li, Z., Yang, Y., et, al. Role of moisture content in coal oxidation during the spontaneous combustion latency. Energy, 2024, 291: 130336.

Liu, R., Ji, D., Zhou, G., et, al. Electrospun nanofibers for personal protection in mines. Chemical Engineering Journal, 2021a, 404: 126558.

Liu, S., Sang, S., Hu, Q., et, al. Characteristics of high-rank coal structure parallel and perpendicular to the bedding plane via NMR and X-ray CT. Petroleum Science, 2020, 17(4): 925-938.

Liu, W., Wang, G., Han, D., et, al. Accurate characterization of coal pore and fissure structure based on CT 3D reconstruction and NMR. Journal of Natural Gas Science and Engineering, 2021b, 96: 104242.

Li, X., Kang, Y., Haghighi, M. Investigation of pore size distributions of coals with different structures by nuclear magnetic resonance (NMR) and mercury intrusion porosimetry (MIP). Measurement, 2018, 116: 122-128.

Li, Z. Evolution of pores and fractures in coal reservoirs and their impact on microscopic flow of coalbed methane. Beijing, China University of Mining and Technology (Beijing), 2018.

Lubelli, B., de Winter, D. A. M., Post, J. A., et, al. Cryo-FIB-SEM and MIP study of porosity and pore size distribution of bentonite and kaolin at different moisture contents. Applied Clay Science, 2013, 80-81: 358-365.

Mazumder, M., Bal, A., Tripathy, A., et, al. Multiscale assessment of transformation in pore system of shale during combustion: An insight into poromechanical response and sorption dynamics. Energy & Fuels, 2024, 38: 17510-17524.

Qin, W., Zhang Y. Relation of pore distribution of coal with water infusion increment in seams. Journal of China Coal Society, 2000(5): 514-517. (in Chinese)

Qin, X., Cai, J., Wang, G. Pore-scale modeling of pore structure properties and wettability effect on permeability of low-rank coal. International Journal of Mining Science and Technology, 2023, 33(5): 573-584.

Raguin, E., Weinkamer, R., Schmitt, C., et, al. Logistics of bone mineralization in the chick embryo studied by 3D Cryo FIB-SEM imaging. Advanced Science, 2023, 10(22): 2301231.

Röding, M., Fager, C., Olsson, A., et, al. Three-dimensional reconstruction of porous polymer films from FIB-SEM nanotomography data using random forests. Journal of Microscopy, 2021, 281(1): 76-86.

Saif, T., Lin, Q., Butcher, A., et, al. Multi-scale multi-dimensional microstructure imaging of oil shale pyrolysis using X-ray micro-tomography, automated ultra-high resolution SEM, MAPS Mineralogy and FIB-SEM. Applied Energy, 2017, 202: 628-647.

Schlüter, S., Sheppard, A., Brown, K., et, al. Image processing of multiphase images obtained via X-ray microtomography: A review. Water Resources Research, 2014, 50(4): 3615-3639.

Sun, Y., Zhao, Y., Wang, X., et, al. Synchrotron radiation facility-based quantitative evaluation of pore structure heterogeneity and anisotropy in coal. Petroleum Exploration and Development, 2019, 46(6): 1195-1205.

Tang, X., Jiang, Z., Jiang, S., et, al. Heterogeneous nanoporosity of the Silurian Longmaxi Formation shale gas reservoir in the Sichuan Basin using the QEMSCAN, FIB-SEM, and nano-CT methods. Marine and Petroleum Geology, 2016, 78: 99-109.

Vierrath, S., Zielke, L., Moroni, R., et, al. Morphology of nanoporous carbon-binder domains in Li-ion batteries-A FIB-SEM study. Electrochemistry Communications,

2015, 60: 176-179.

Vranjes-Wessely, S., Misch, D., Issa, I., et, al. Nanoscale pore structure of Carboniferous coals from the Ukrainian Donets Basin: A combined HRTEM and gas sorption study. International Journal of Coal Geology, 2020, 224: 103484.

Wang, C., Li, X., Liu, L., et, al. Dynamic effect of gas initial desorption in coals with different moisture contents and energy-controlling mechanism for outburst prevention of water injection in coal seams. Journal of Petroleum Science and Engineering, 2023, 220: 111270.

Wang, G., Chen, X., Cheng, W., et, al. Multi-scale characterization of coal pore and fractures and its influence on permeability-taking 14 large coal bases in China as examples. Journal of Chongqing University, 2024, 47(4): 34-50. (in Chinese)

Wang, G., Chen, X., Wang, S., et, al. Influence of fracture connectivity and shape on water seepage of low-rank coal based on CT 3D reconstruction. Journal of Natural Gas Science and Engineering, 2022, 102: 104584.

Wang, G., Shen, J., Liu, S., et, al. Three-dimensional modeling and analysis of macro-pore structure of coal using combined X-ray CT imaging and fractal theory. International Journal of Rock Mechanics and Mining Sciences, 2019, 123: 104082.

Wang, H., Cheng, X., Tian, J., et, al. Permeability enhancement of low rank coal through acidization using H_2S solution: An experimental study in the Kuqa-Bay Coalfield, Xinjiang, China. Journal of Petroleum Science and Engineering, 2020, 185: 106476.

Wang, W., Teng, T. Experimental study on anisotropic fracture characteristics of coal using notched semi-circular bend specimen. Theoretical and Applied Fracture Mechanics, 2022, 122: 103559.

Wu, J., Yuan, Y., Niu, S., et, al. Multiscale characterization of pore structure and connectivity of Wufeng-Longmaxi shale in Sichuan Basin, China. Marine and Petroleum Geology, 2020, 120: 104514.

Yang, W., Lu, C., Si, G., et, al. Coal and gas outburst control using uniform hydraulic fracturing by destress blasting and water-driven gas release. Journal of Natural Gas Science and Engineering, 2020, 79: 103360.

Yu, B., Dijkstra, T. A., Fan, W., et, al. Advanced multi-scale characterization of loess microstructure: Integrating μXCT and FIB-SEM for detailed fabric analysis and geotechnical implications. Engineering Geology, 2024, 341: 107727.

Zang, J., Liu, J., He, J., et, al. Characterization of the pore structure in Chinese anthracite coal using FIB-SEM tomography and deep learning-based segmentation. Energy, 2023, 282: 128686.

Zhang, C., Jia, S., Wang, F., et, al. An experimental research on the pore and fracture evolution characteristics and its driving mechanism for coal samples under water-rock interaction. Journal of Basic Science and Engineering, 2023, 31(1): 185-96.

Zhang, R., Liu, S., San-Miguel, A., et, al. Nanoscale coal deformation and alteration of porosity and pore orientation under uniaxial compression: An in situ SANS study. Rock Mechanics and Rock Engineering, 2021, 54(7): 3593-608.

Zhang, X. Fractal character of coal nanopore and effect of deviation corrected, coal rank, and gas adsorption. Microporous and Mesoporous Materials, 2024, 367: 112972.

Zhao, Y., Sun, Y., Liu, S., et, al. Application of fractal theory to predict the coal permeability of multi-scale pores and fractures. Energy Reports, 2018, 7(2): 10-18.

Zheng, L. Mechanism and engineering application of hydraulic fracturing, permeability enhancement, wetting and dust suppression in difficult-to-inject coal seams. Chongqing, Chongqing University, 2022.

Zhou, F., Oraby, M., Luft, J., et, al. Coal seam gas reservoir characterisation based on high-resolution image logs from vertical and horizontal wells: A case study. International Journal of Coal Geology, 2022, 262: 104110.

Zhou, H., Liu, Z., Zhao, J., et, al. *In-situ* observation and modeling approach to evolution of pore-fracture structure in coal. International Journal of Mining Science and Technology, 2023, 33: 265-274.

Zhou, Y., Zhong, X., Nie, X. Identification and parameter characterization of pores and fractures in shales based on multi-scale digital core data. Advances in Geo-Energy Research, 2024, 13(2): 146-160.